BUTTERWORTH HEINEMANN

Polymer Vol. 36 No. 25, pp. 4771–4786, 1995

0032-3861/95/$10.00+0.00

Microstructural processes of fracture of rubber-modified polyamides

O. K. Muratoğlu*, A. S. Argon† and R. E. Cohen‡
Massachusetts Institute of Technology, Cambridge MA 02139, USA

and M. Weinberg
E. I. de Pont de Nemours & Company, Central Research and Development Department, Experimental Station, Wilmington, DE 19898, USA
(Received 17 January 1995; revised 19 May 1995)

The microstructural processes of fracture in rubber-modified polyamides were studied in blends of polyamide 66/ethylene–propylene–diene rubber (PA66/EPDR) in Izod bending impact experiments. Izod tests were performed at various temperatures to determine the ductile–brittle transition as a function of temperature, rubber weight fraction and particle size. Subsequent analysis of the fracture surfaces by scanning electron microscopy revealed unique morphologies for various regions of toughness: in the brittle region, the fracture surface is patchy; in the transition region, there are occasional striations present on the fracture surface, along with the brittle fracture morphology; in the tough region, the fracture surface is fully covered by striations which penetrate only $\sim 2\,\mu$m beneath the surface in the form of shallow cracks perpendicular to the surface. The striations lie parallel to the main crack front and are a signature of the effective toughening of the polyamide through the incorporation of rubber particles. This drastic change in the fracture surface morphology and formation of striations at the ductile–brittle transition point is the result of elastic–plastic buckling of previously highly stretched material layers on the crack flank as they undergo a constrained accommodation. Morphological studies of the process zone, mainly below the crack flanks, have confirmed this hypothesis of buckling of surface layers. The spacing between the striations observed on the fracture surface of tough specimens varied with rubber content, particle size, temperature and strain rate. These effects are discussed in terms of local adiabatic heating and variations in the plastic resistance of the matrix material. A model for striation formation based on plastic buckling of a thin surface layer on a porous elastic foundation is provided that serves as a scaling relation accounting well for the temperature-dependent changes in striation spacing.

(Keywords: rubber-modified polyamide; fracture; striation formation; model)

INTRODUCTION

Polyamides are strong engineering polymers. They exhibit high resistance to crack initiation, which imparts high toughness to unnotched material. However, their low resistance to crack propagation[1] leads to embrittlement in the presence of a notch that results in high local strain rates. Upon modification with rubbery inclusions, the resistance to crack propagation increases, leading to super-tough materials. This toughening procedure by the incorporation of submicrometre-sized rubber particles has been extensively studied[2–7]. The effects of rubber concentration[8], particle size[8,9] and interparticle distance[3] on the toughening process are well documented: increasing the concentration of rubber particles, decreasing the particle size or decreasing the interparticle distance all improve the toughness. Wu showed that at a critical interparticle ligament thickness, independent of rubber concentration and particle size, there exists an abrupt transition from ductile to brittle behaviour with increasing ligament size[3]. This transition is reported to occur around a ligament thickness of 0.3 μm in rubber-modified polyamide 66[3].

Several mechanisms have been proposed to explain this abrupt transition. Recently, Muratoğlu *et al.*[10] demonstrated that the rubber–polyamide interface significantly alters the morphology of the crystallization process that has important consequences on the toughness transition. The hydrogen-bonded crystallographic planes of the matrix preferentially align parallel to this interface, creating an oriented skin layer around the rubber particles. This preferred orientation has been observed in polyamide 6[10], polyamide 66[11,12] and polyamide 610[11]. When the interparticle distance in a rubber-modified polyamide is decreased sufficiently, the skin layers overlap, and a critical fraction of the matrix assumes a preferred orientation of hydrogen-bonded planes parallel to the rubber–matrix interfaces[13]. Lin and Argon[14] have shown that the hydrogen-bonded planes of polyamides possess the lowest resistance to slip. Therefore, the oriented crystalline regions exhibit

* Program in Polymer Science and Technology and Department of Material Science and Engineering
† Department of Mechanical Engineering. To whom correspondence should be addressed
‡ Department of Chemical Engineering

varying flow stresses depending on the direction of the applied load relative to the hydrogen-bonded planes. In some regions of ligaments where the skin layers overlap, the plastic resistance is significantly reduced. As long as regions with such orientation percolate through the material, early fracture processes are avoided and the material is tough; this 'catastrophe avoidance' approach to toughening of polyamides has been described in detail elsewhere[13].

The above-mentioned approach to toughening does not directly address the intrinsic fracture process. Nevertheless, the rubber modification and its attendant local preferred orientation imparts to polyamides a high resistance to crack propagation and enhanced toughness. While much has been learned from such previous studies, ultimately it is important to study the crack propagation to understand the underlying mechanism in action which is responsible for the increase in the resistance to crack propagation. Dijkstra *et al.*[15] have studied the effect of strain rate and temperature on the crack initiation and propagation of rubber-modified polyamide 6. Based on measurements of fracture energy during crack propagation in a singly notched tensile specimen, they concluded that the resistance to crack propagation in rubber-toughened polyamide 6 was due to localized melting in the process zone that resulted in the thermal blunting of the crack tip. In the present study, we have investigated the local fracture process in notched Izod flexural bars. The detailed analysis of the fracture surface and the zone of intense plastic deformation of the crack flanks has provided a new level of understanding of the operating microstructural processes that occur during crack propagation in rubber-toughened polyamide 66.

EXPERIMENTAL

Sample preparation and characterization

A 28 mm Werner & Pfleiderer extruder was used to blend polyamide 66 with maleic anhydride functionalized ethylene–propylene–diene rubber. The functionality levels were varied to obtain a range of particle sizes. The resulting blends were pelletized and then moulded in a 6 oz, 150 ton Van Dorn injection moulding machine into flexural test bars (length = 127 mm, width = 12.5 mm, thickness = 3.2 mm). The Izod bars were cut from the middle part of the flexural bars. Notches were introduced into each part with a TMI Notching Cutter according to the specifications of ASTM D256. Following the injection moulding and notching process, the samples were placed in air-tight bags and stored in a dessicator to prevent the absorption of water. To determine the particle size of rubber inclusions, small-angle X-ray scattering (SAXS)[16] and scanning electron microscopy (SEM) techniques were used. *Table 1* summarizes the sample characteristics.

Izod impact test

The Izod impact tests were conducted at various temperatures on dry, as-moulded samples. Prior to testing, flexural bars were conditioned in a sealed chamber immersed in a heating or a cooling bath to achieve the desired sample temperature. The samples were heated or cooled under a flow of dry argon gas to avoid further absorption of water. All samples were handled according to exactly the same procedures in an effort to ensure that they all contained essentially the same concentration of water. Izod values reported in this study the average of five tests.

Table 1 Sample characteristics

Sample no.	Rubber concentration (wt%)	Particle diameter (μm)
1	0	–
2	5	0.19[a]
3	10	0.17[a]
4	15	0.17[a]
5	20	12.00[b]
6	20	1.10[b]
7	20	0.63[a]
8	20	0.32[a]
9	20	0.17[a]

[a] SAXS values
[b] ESEM values

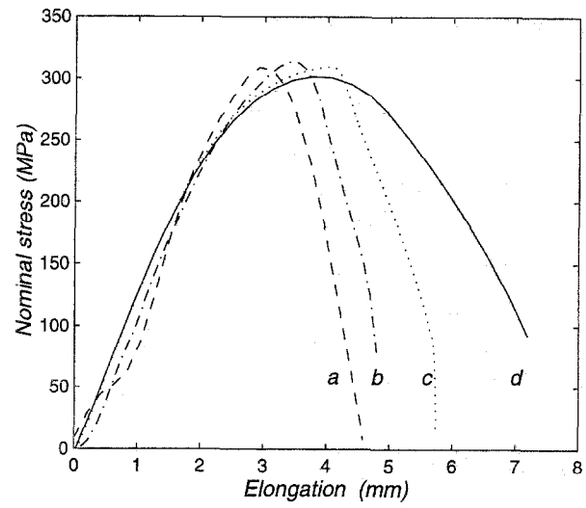

Figure 1 Nominal stress–elongation curves of singly notched tensile tests of sample 8 (total length of specimen is 127 mm) at crosshead speeds of (a) 500, (b) 100, (c) 10 and (d) 1 mm min^{-1}, corresponding to crack velocities of 5, 1, 0.1 and 0.005 cm s^{-1}

Single-notch tensile test

The notched Izod flexural bars of sample 8 were also tested in uniaxial tension in an Instron 4200 universal testing machine. The crosshead speeds used were 1, 10, 100 and 500 mm min^{-1}. *Figure 1* shows the corresponding load–displacement curves. While the load in the specimen increases, a crack initiates at the tip of the notch. This is followed by the propagation of a crack that starts when the load reaches the maximum level, beyond which the crack travels at a constant velocity governed by the crosshead speed. The relation between the average crack velocity v_c, the nominal displacement required for full fracture d_p and crosshead speed v_{ch} is as follows:

$$v_c = \frac{r}{d_p/v_{ch}} \quad (1)$$

where r is the distance travelled by the crack. In this case r is simply the distance t from the tip of the notch to the edge of the sample, since the experiment is carried out to total fracture. Using the above equation, the corresponding crack velocities attained in crosshead speeds of 1, 10,

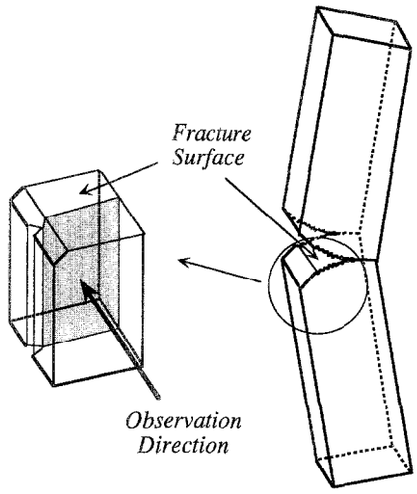

Figure 2 Schematic of the cryo-fracture method to view the process zone and fracture surface morphologies: a wedge is driven into the notch at liquid nitrogen temperature. The shaded surface is coated with Au and examined in an SEM

100 and 500 mm min^{-1} are calculated to be 0.005, 0.1, 1 and 5 cm s^{-1}, respectively. Thus, the progressive fracture or separation of the sample shows no instability, and reflects the behaviour of a very tough material with a very high tearing resistance.

Scanning electron microscopy

Following the Izod and single-notch tensile tests, the samples were examined in a scanning electron microscope (SEM) to determine the fracture surface features and changes in morphology of the cavities within the process zone; the parameters of the study were temperature, rubber concentration and particle size for the Izod tests, and crack propagation velocity for the single-notch tensile tests. To view the morphology of cavities in the stress-whitened zone below the crack flanks, the samples were cryo-fractured along a median plane from a notch cut perpendicular to the original Izod notch as shown in *Figure 2*. A similar method to examine the internal cavitation in rubber-modified polyamide 6 has been used by Speroni *et al.*[17] Primary fracture surfaces and the cryo-fractured surfaces of specimens were coated with a thin layer of Au and examined in an Elektroscan

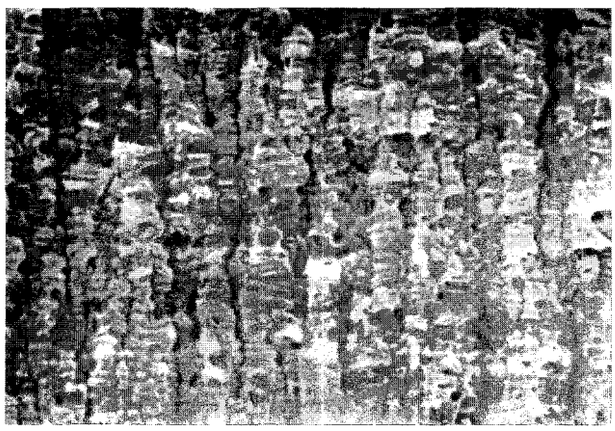

(a)

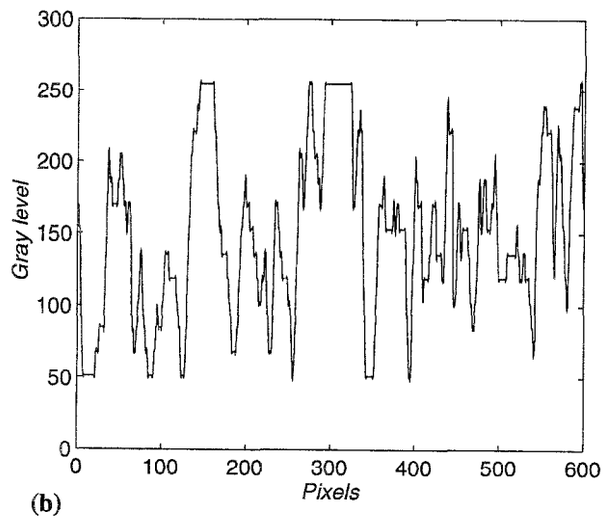

(b)

Figure 3 Scanning step of the image analysis procedure: (a) scanned image of the fracture surface micrograph of sample 9 tested at 60°C; (b) grey level profile of the top horizontal border of the figure

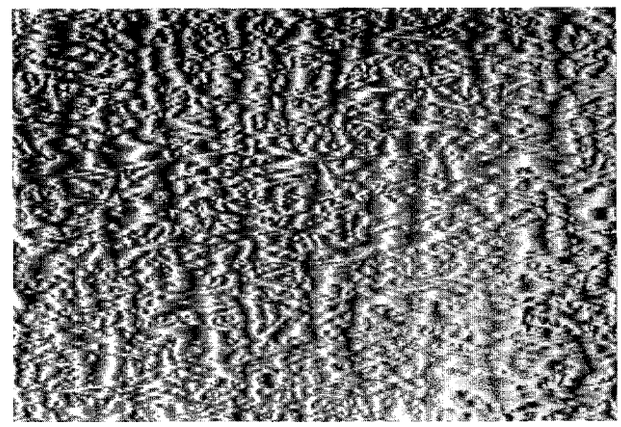

(a)

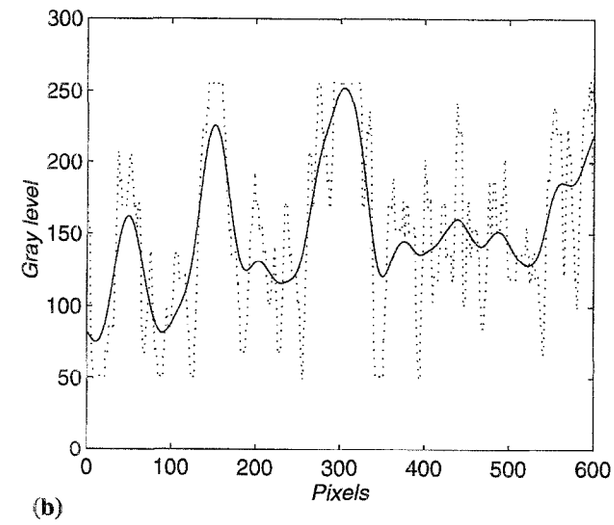

(b)

Figure 4 Smoothing step of the image analysis technique: (a) smoothed image of *Figure 3a*, resulting from the smoothing of all line scans in the manner described in the text; (b) smoothed (solid curve) and as-scanned (dashed curve) profiles of the top horizontal border of the figure

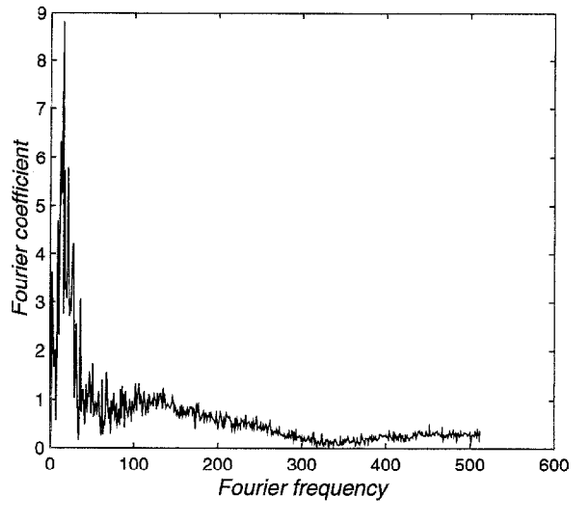

Figure 5 Fast Fourier transform of the smoothed fracture surface micrograph (*Figure 4a*) of sample 9 tested at 60°C. The transform is the average of individual transforms of ~600 horizontal lines constituting the image

environmental scanning electron microscopy (ESEM). The instrument used a caesium hexaboride filament operated at an accelerating voltage of 15 kV.

Image analysis

The distribution of striation spacing on the primary fracture surface of tough specimens was determined by taking the fast Fourier transforms (FFTs) of the fracture surface micrographs. The method used for the FFTs consisted of: scanning the micrographs at a scan resolution of 300 dots per inch (dpi) and rotating the scanned images such that the striations are vertical as shown in *Figure 3a*. Scanning divides the image into pixels and assigns them integers between 0 and 255 depending on the level of grey, where 0 is white and 255 is black. *Figure 3b* shows the intensity profile along one horizontal line—the top border of the scanned image is shown in *Figure 3a*. The striations in the image give rise to fluctuations in the intensity profile of the scan. Along each line splines are fitted to smooth the image as shown in *Figure 4a*. The intensity profile of the top line after smoothing is plotted in *Figure 4b* along with the raw profile. The FFT of each line was then taken and Fourier coefficients were plotted as a function of Fourier frequencies. As an example, *Figure 5* shows the transform of the fracture surface of sample 9 tested at 60°C.

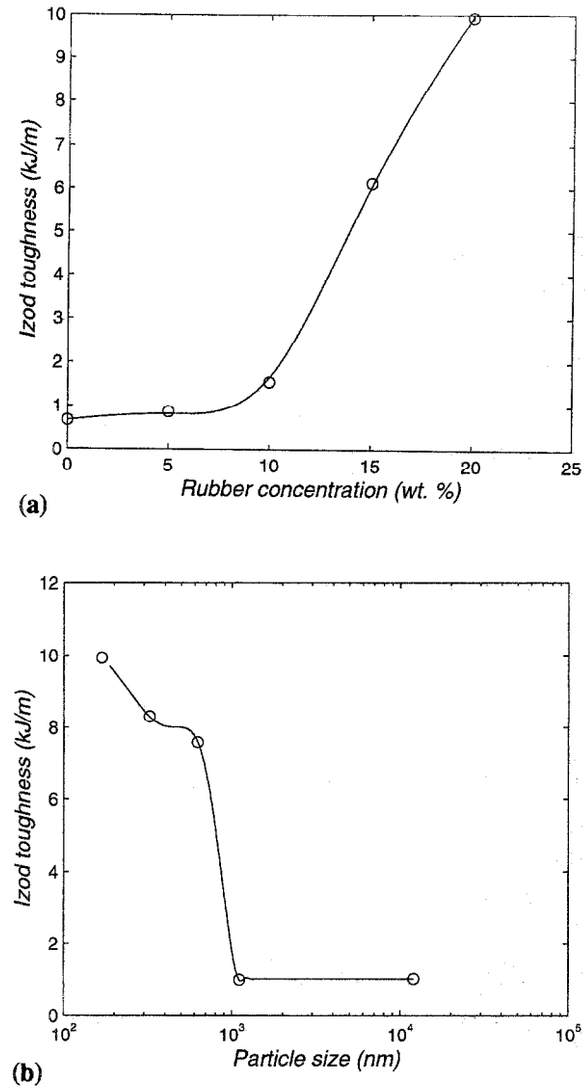

Figure 6 Effect of (a) rubber concentration and (b) particle size on Izod toughness, determined at room temperature

The peak is taken to be the mean frequency of the striations on the fracture surface. The frequency–distance conversion is established using the following equation:

$$S_d = C\frac{n\nu}{(dpi)M} \tag{2}$$

Table 2 Izod toughness values[a] ($J\,m^{-1}$) at various temperatures (°C)

Sample no.	−14	0	20	30	40	50	60	70	80
1	–	–	700	–	–	–	–	–	1400
2	–	–	900	–	–	1000	1000	4500	5300
3	–	1400	1600	1900	6100	5200	6400	–	–
4	800	5500	6100	6300	7100	9000	10900	–	–
5	–	–	600	–	–	–	–	–	600
6	–	1100	1000	1000	1100	1200	1500	4500	–
7	800	4900	7600	5200	6900	8100	14200	–	–
8	700	7000	8300	8200	8300	14700	–	–	–
9	900	7300	9900	8200	8500	9600	17600	–	–

[a] Average of five tests at each temperature. Error bars are typically ±5%

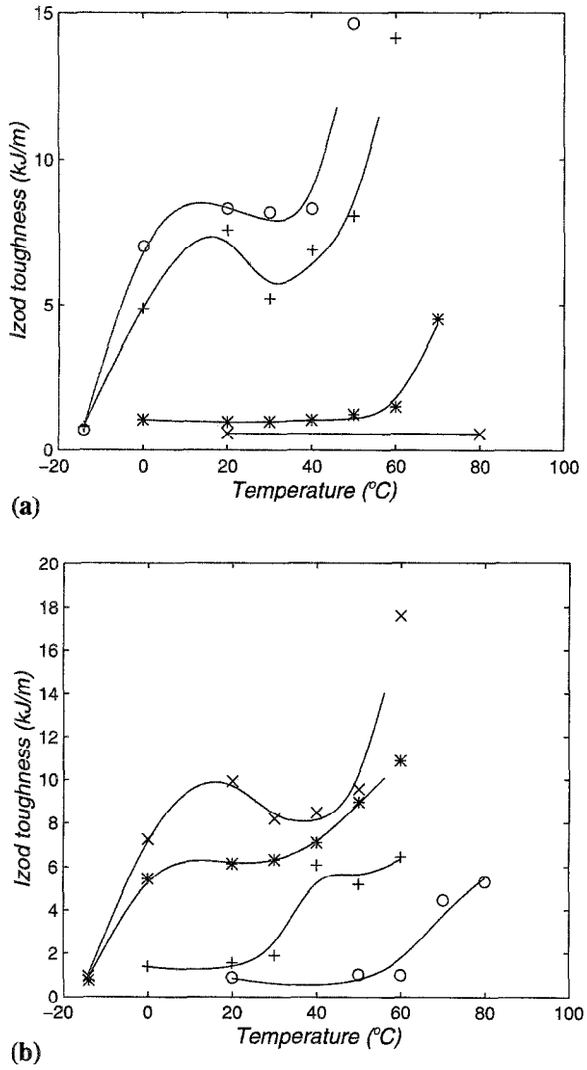

Figure 7 Effect of temperature on Izod toughness at: (a) constant rubber concentration of 20 wt% with a particle size of (○) 0.32 μm, (+) 0.63 μm, (*) 1.12 μm, (×) 12 μm; and (b) at constant particle size of ~0.17 μm with a rubber content of (×) 20, (*) 15, (+) 10 and (○) 5 wt%

where S_d is the striation spacing in μm, n is the number of pixels along one line, *dpi* is the scanning resolution in dots per inch, M is the magnification of the scanned micrograph, ν is the Fourier frequency, and C (= 2.54×10^4) converts from inches to μm.

RESULTS AND DISCUSSION

The central purpose of the present research was to study the microstructural processes involved in the fracture of rubber-modified polyamide 66 via morphological analyses of the fracture surfaces and process zones. During the deformation of these rubber-toughened polymers, the particles cavitate at a critical stress and cause the observed whitening in the deformation zone. Several studies[13,17] have already shown that under various straining modes, the cavities elongate in the principal direction of extension while the interparticle regions of the matrix deform to draw ratios of about 8 and form microfibrils. Only the tensile specimens that are able to form a stable neck exhibit the desirable microfibrillation of the matrix which is found to be an indication of effective toughening[13]. The analysis of the fracture process in Izod impact specimens subsequent to this cavitation and microfibrillation is reported below.

Izod impact test results

The results of Izod impact tests performed on various samples at different temperatures are reported in *Table 2*. Some samples were not tested at certain temperatures where their toughness values were below the lower or above the upper (brittle or ductile) bounds. The results are plotted in *Figures 6* and *7*. As seen in *Figure 6*, toughness increases as the rubber concentration increases or as the particle size decreases. In both cases there exists a ductile–brittle transition. Previous studies have shown that the location of this transition is a function of temperature[8]. *Figures 7a* and *b* show the effect of temperature when the other two parameters are held constant. The ductile–brittle transition temperature decreases as the particle size decreases at a constant rubber fraction of 20 wt% (*Figure 7a*), whereas it increases as the rubber fraction decreases at a constant particle size of around 0.17 μm (*Figure 7b*). These results are in accord with findings reported in the literature[8,9], and consistent with the concept of percolation of preferentially oriented material in interparticle ligaments[13].

Fracture surface morphology

To gain a better understanding of how the microstructural failure processes interact with a growing crack, the fracture surface morphology of the Izod samples was examined in an ESEM. Three distinctive features, namely (a) a patchy surface, (b) striations and (c) a combination of (a) and (b), were found to predominate on the fracture surfaces. *Figure 8* summarizes these different forms in the fracture surface features and identifies them in relation to the observed levels of toughness. In the brittle region, the fracture surface exhibits a macroscopically smooth surface with irregular features which are typical to the brittle failure[18] (see *Figure 8b*). The fracture surfaces of all the ductile specimens are fully covered with striations (*Figure 8d*), while the specimens in the transition region (*Figure 8c*) show a combination of the irregular-patchy brittle fracture surface and striations. In the micrographs included in *Figure 8*, the direction of crack propagation is from left to right. The variable on the abscissa of the inserted schematic graph of the toughness level (*Figure 8a*) could be alternatively the rubber weight fraction, or the inverse particle size. In all cases, the evolution of fracture surface morphology with toughness is identical. That is, the type of fracture surface morphology generated by the propagating crack depends only on the level of toughness of the sample and not explicitly on the particle size, rubber fraction or temperature of fracture, while these factors, of course, establish the appropriate level of toughness. Therefore, the drastic transition from a fracture surface with irregular features to a fracture surface with regularly spaced striations is solely due to the variations in the toughness level. To gain more insight in understanding the toughening of these materials, it is necessary to relate the evolution of the fracture process to the formation of the striations in tough samples to establish a mechanistic connection.

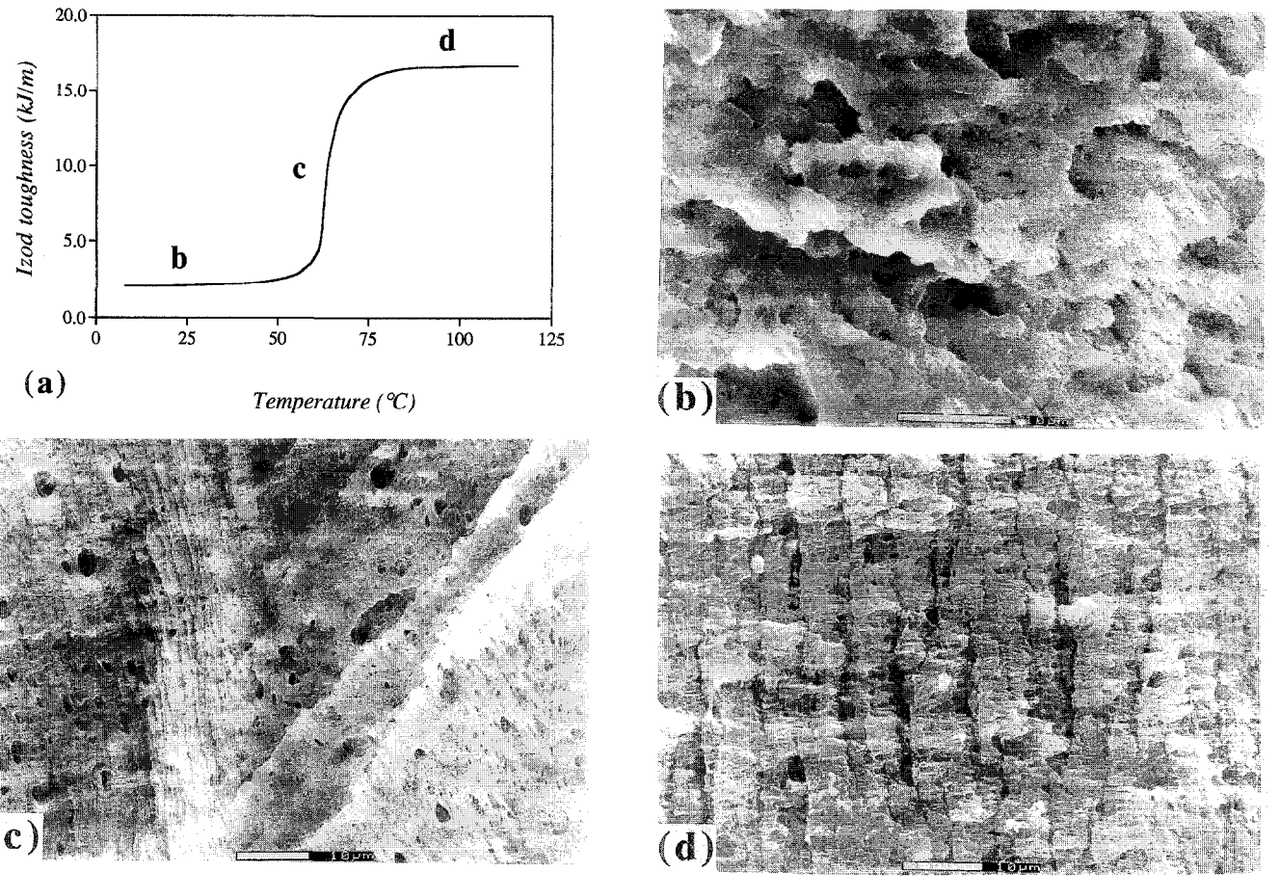

Figure 8 Evolution of fracture surface morphology, related to levels of Izod toughness: (a) schematic variation of the toughness level with temperature; (b), (c) and (d) representative fracture surface morphologies of samples from regions of toughness as indicated in (a)

Striations in impact and fatigue fracture

The type of brittle fracture surfaces encountered in this study have been widely reported for other materials with 'granular' microstructure under brittle modes of failure. Striations have also been observed in ductile impact fracture of polyamides. The fracture surface micrographs reported in refs 1 and 9 show striations that were not mentioned by the authors. For instance, Figure 12 of ref. 1 depicts the impact fracture surface of a toughened polyamide exhibiting striations that are $\sim 6\,\mu m$ apart. Similarly, Figure 4a of ref. 9 shows an impact fracture surface micrograph of a rubber-toughened polyamide 66 where the striations are discernible. Recently, Speroni *et al.*[17] showed that striations parallel to the crack front coexist with 'fish-bone' shear bands on impact fracture surfaces of water conditioned homo-polyamide 6. They also observed that rubber modification suppresses the formation of 'fish-bone' shear bands and the fracture surfaces are fully covered by striations. Upon examining the substrate morphology of the flanks they noted that the elongated cavities are inclined at an angle of 20° to the fracture surface and intersect the direction of cavitation fronts at an angle of ~76°; hence they proposed that the striations are formed as a consequence of interaction of shear bands with the crack surface. However, the micrograph (Figure 15f of ref. 17) shows that the substrate morphology of the flanks must have resulted from extensive buckling of the elongated cavities near the crack flank, suggesting deformation of a thin layer on the fracture surface undergoing an instability.

The striations have often been associated with fatigue fracture surfaces, where they indicate the intermittent, cyclic propagation of the fatigue crack. In some instances, the distance between these arrest lines is not the same as the average cyclic crack-growth increments[19–21]. If the incremental advancement of the crack occurs after several cycles, the spacing of the fracture lineage will be larger than the macroscopic crack-growth increments[22]. Particular semicrystalline[23] as well as glassy polymers[22] exhibit this so-called discontinuous crack growth. Conversely, some polymers display regular lines on fatigue fracture surfaces with spacings smaller than the cyclic crack-growth increments.

For instance, in fatigue crack propagation experiments on polyamide 66 and its rubber-toughened grades, Hahn *et al.*[20] observed both a patchy fracture surface and a 'rumpled' one depending on the level of the stress intensity factor. The former corresponds to the brittle fracture surface type observed in this study, while the latter is identical to the regularly spaced striations shown in *Figure 8d*. They found that the transition from the patchy surface to the 'rumpled' one occurs with increasing water content, rubber concentration, and test frequency; the spacing between the rumples varied with water content and rubber concentration at a constant test frequency. This observation implies that the 'rumples' are not formed by the intermittant cyclic crack growth but by another mechanism. Hahn *et al.*[20] proposed a model where secondary cracks, in the form of fissures perpendicular to the main crack plane, form

ahead of the propagating crack tip due to the delamination of highly stretched material. As fracture proceeds the oriented material between the fissures fractures and gives rise to the 'rumpled' fracture surface. However, the authors did not provide any direct evidence of fissure formation in front of the crack tip.

In another study, White and Teh[21] examined fatigue fracture surfaces of low density polyethylene, and found that the expected 8 μm/cycle growth increments are much larger than the average 'micro-striation' spacing of 0.5 μm (at room temperature). Under a higher amplitude tensile strain cyclic loading the fracture surface consisted of macro-striations with spacings corresponding to cyclic crack-growth increments and micro-striations lying between macro-striations. White and Teh proposed a mechanism for the formation of micro-striations: the crystalline lamellae are oriented parallel to the crack front and perpendicular to the crack flank, so that, when the crack propagates, the previously oriented lamellae fracture and leave features on the fracture surface that are identified as micro-striations. However, the spacing of the observed micro-striations (~0.5 μm) is much larger than the average lamellar thickness of polyethylene (~10 nm)[19], leaving this model of questionable validity. In a following section a hypothesis is presented, based on morphological observations, for the formation of similar striations (also observed by Speroni *et al.*[17] on impact fracture surfaces) formed upon impact fracture in rubber-modified polyamides.

Morphology of striations in impact fracture

The striations on the fracture surface of ductile specimens have the distinct appearance of shallow grooves perpendicular to the surface of the crack flank and lie parallel to the crack front. *Figure 9* gives a schematic view of striations on a fracture surface, where they are depicted as a square wave of amplitude a and wavelength S_d. *Figures 10a* and *b* depict the typical striations formed at temperatures of 20 and 50°C, respectively, during the Izod impact test of specimens of sample 8. In these micrographs, recorded under conditions of high contrast, the striations appear to penetrate deep into the fracture surface. To obtain a better view of the actual depth of penetration, the samples were cryo-fractured following the method described in the Experimental section and depicted in *Figure 2*. A representative micrograph is displayed in *Figure 11*, from which it is quite clear that the striations

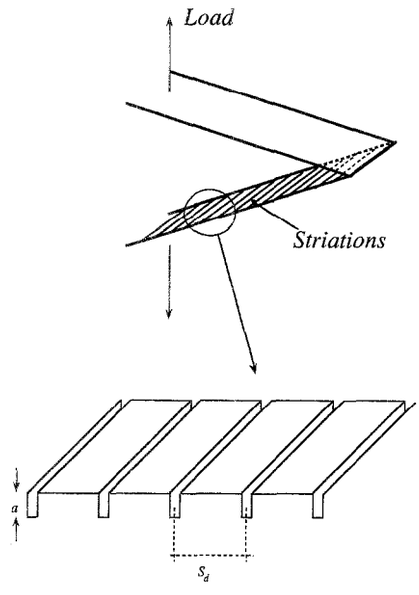

Figure 9 Schematic of striations left on the fracture surfce of a tough specimen during fracture. The striations are parallel to the propagating crack front

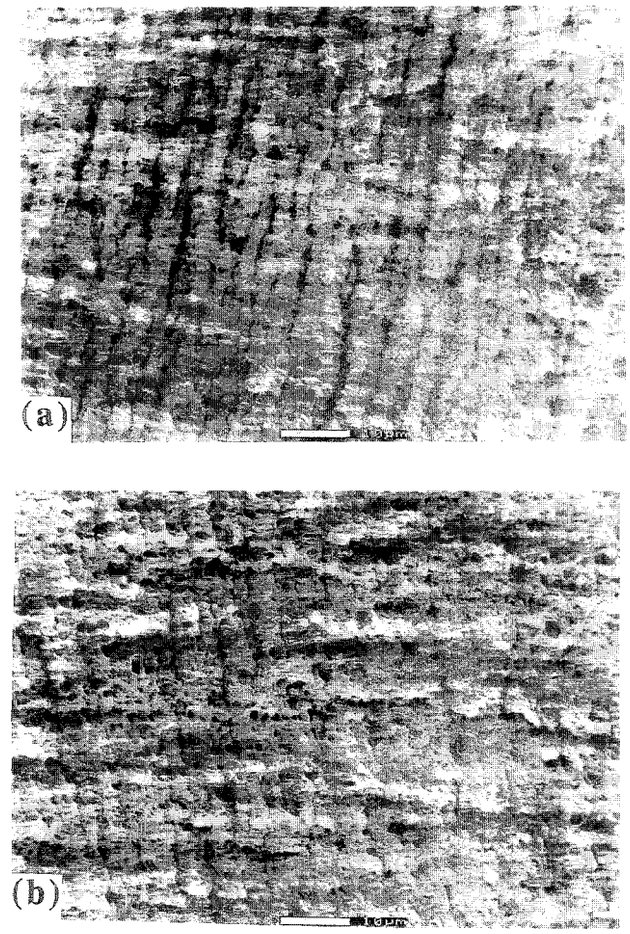

Figure 10 Fracture surface of sample 8 tested at (a) 20 and (b) 50°C. The direction of crack propagation is from left to right

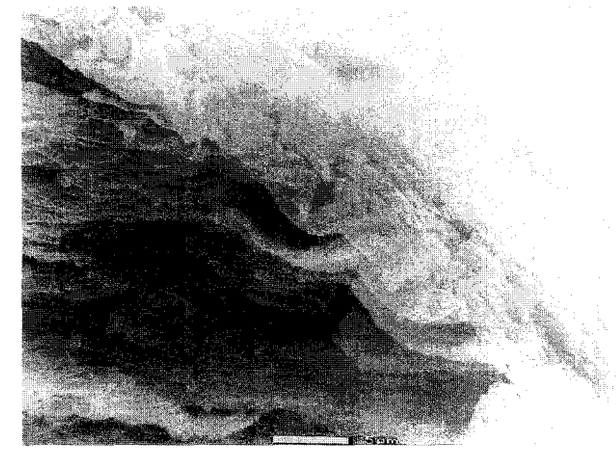

Figure 11 Side view of a crack flank showing a set of striations. The direction of crack propagation is from left to right

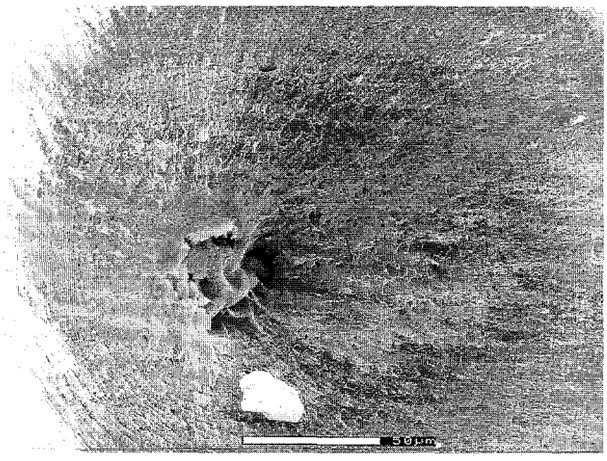

Figure 12 Striations on the fracture surface of sample 9, showing an example of a secondary crack in the plane of the main cracking event

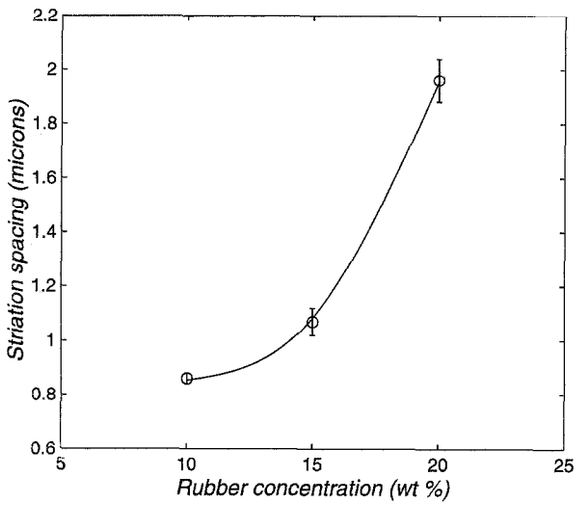

Figure 13 Variation of striation spacing with rubber concentration measured on the fracture surface of specimens fractured at 60°C, via the image analysis technique described in the Experimental section (rubber particle size is constant at ~0.17 μm)

are surface folds that do not penetrate deeply into the sample. The approximate depth of penetration as measured from such a micrograph is ~2 μm.

The striations are not only created by the propagation of the main crack. They were also associated with secondary cracks which initiate from separate fracture nuclei and propagate radially outwards, within the main crack plane. *Figure 12* gives a clear example of such nucleation of a secondary crack and its radial outward propagation, where the striations indicate the direction of the radial crack propagation. Eventually, the secondary crack meets the main crack and the fracture process proceeds with the opening of the former. Such secondary nuclei are well known in the fracture surfaces of glassy[24–26] and semicrystalline polymers[21] where they give rise to the ubiquitous parabola, studied by many investigators.

Table 3 Striation spacings on fracture surfaces of Izod impact samples

Temperature	Striation spacing (μm)[a] of samples					
(°C)	2	3	4	7	8	9
0	–	–	0.70	3.95	2.22	1.00
20	–	–	0.59	3.70	1.75	0.90
30	–	–	0.69	4.34	1.05	0.72
40	–	–	–	4.01	2.68	1.98
50	–	–	1.11	5.20	4.98	2.00
60	–	0.86	1.07	3.21	–	1.96
80	1.35	–	–	–	–	–

[a] Error bars are typically ±1%, based on the breadth of distribution of the Fourier frequencies (transformed to real space) discussed in the Experimental section

Parameters affecting the inter-striation distance

Fracture surface analysis of various samples revealed that while the depth of penetration of the striations remains unchanged, the striation spacing S_d varies with the rubber content, particle size, temperature and deformation rate. The S_d values measured by the image analysis technique described above are listed in *Table 3* for samples exhibiting tough behaviour (hence striations) within the temperature range covered in this study. *Figure 13*, a plot of S_d *versus* the rubber content, demonstrates that the striation spacing increases in samples with higher rubber concentrations. The values of striation spacing measured from the series of samples with a constant rubber content and varying particle size are plotted in *Figure 14*. In this case, the spacing between striations increases with increasing temperature and the curves are shifted up for samples with larger rubber particles. The shape of curves of constant particle size suggests an effect of transition in the formation of the striations at around 30–50°C. The effect of deformation rate on the striation spacing could not be ascertained from Izod tests. Therefore, single-notch tensile tests were carried out on specimens of sample 8 at various cross-head speeds of 1, 10, 100 and 500 mm min^{-1} resulting in crack velocities of 0.005, 0.1, 1 and 5 cm s^{-1}. *Figure 15* displays the fracture surface morphologies of these specimens. The distance between the striations increases

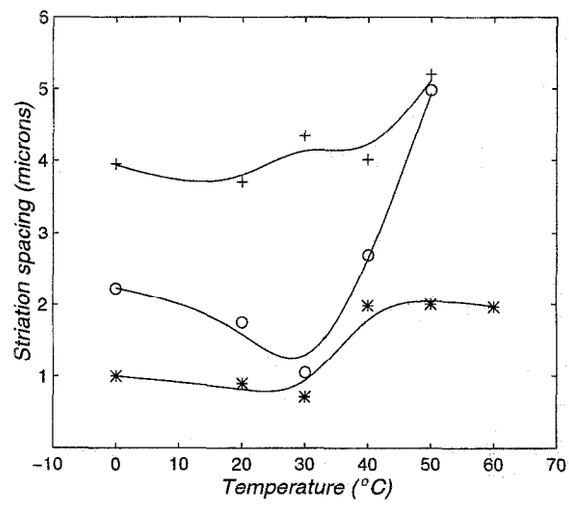

Figure 14 Variation of striation spacing with temperature as measured on the fracture surface of specimens of sample 7 (+), 8 (○) and 9 (*), via the image analysis technique described in the Experimental section. All samples had the same rubber content (20 wt%) and the particle size varied as follows: 0.63 μm (+), 0.32 μm (○), 0.17 μm (*). The error bars are left out of this plot, because they are the same size as the plot symbols

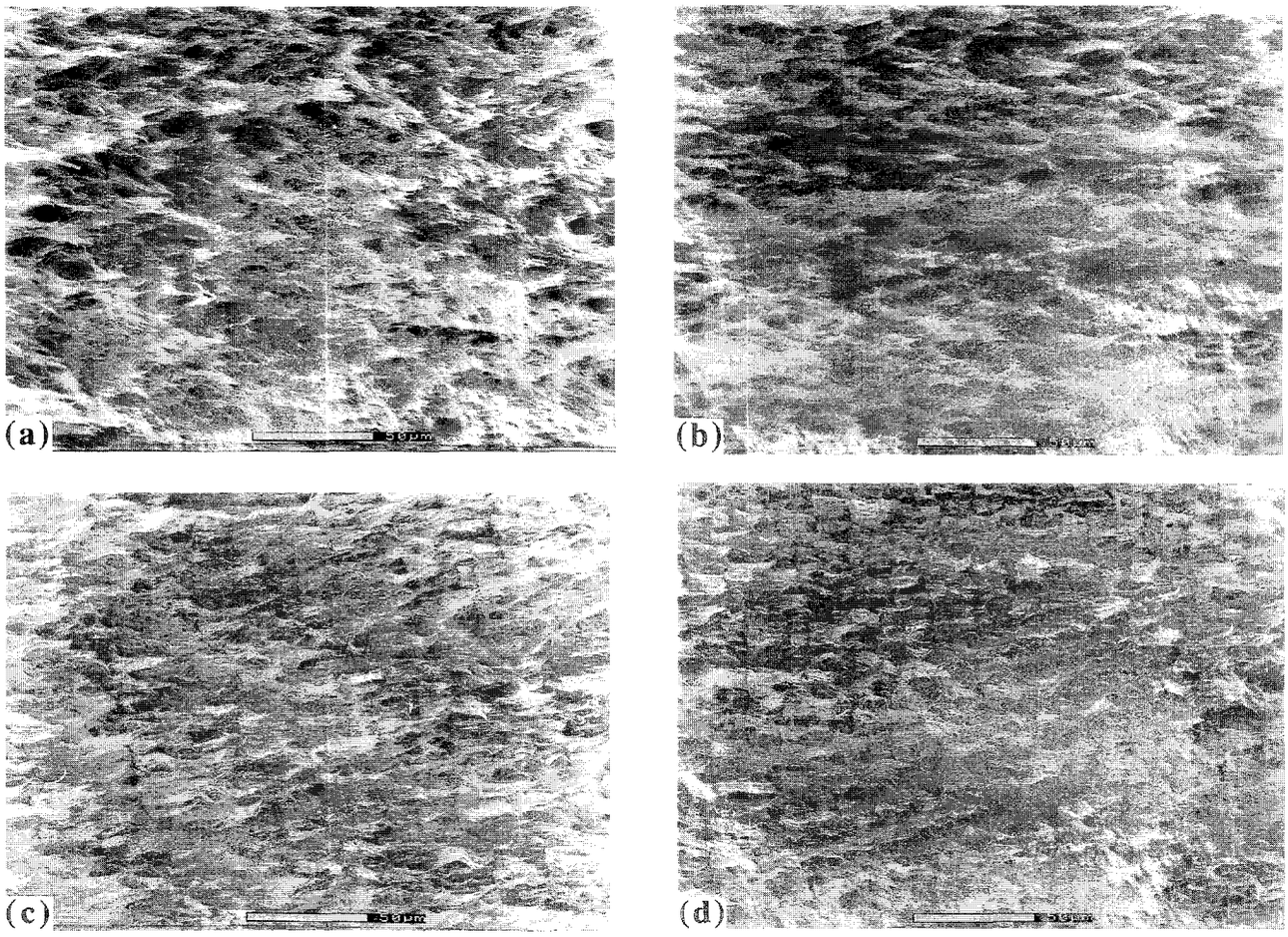

Figure 15 Fracture surface micrographs of specimens of sample 8 after the single-notch tensile tests at crack velocities of (a) 0.005, (b) 0.1, (c) 1 and (d) 5 cm s^{-1}. The direction of crack propagation is from left to right

with decreasing crack velocity. When the velocity of the crack is around 0.005 cm s^{-1} the striations are not even discernible on the fracture surface. The variations in the striation spacing with temperature and deformation rate are a consequence of localized adiabatic heating during deformation and its attendant effects on local plastic resistance of the matrix, which will be discussed in a later section.

Hypothesis for the formation of striations

The characteristics of the observed fracture surface striations in rubber-toughened polyamide 66 have been described but the mechanism that produces them requires clarification. One possibility is that they are the result of the dynamic effects of impact testing investigated in detail by Williams[27], who demonstrated clearly that oscillations of a fracturing, relatively compliant, specimen struck by the pendulum could produce intermittent crack advance and could lead to totally non-representative behaviour in an impact test. If such oscillations are produced in the Izod test, the crack could propagate intermittently, generating arrest lines on the fracture surface. In the Williams phenomenon the oscillations are damped out and full contact is achieved soon after the beginning of the fracture process. Thus, if such oscillations were the cause of the striations, the amplitude of the folds seen in *Figure 11* should diminish and the striations should become less distinct as the crack proceeds in its growth over the fracture surface. In the present case, the striation spacings measured on various specimens remained constant throughout the fracture surface, ruling out the possibility of transient oscillations.

A more consistent explanation for the formation of the striations is the regular elastic–plastic buckling of a thin and stretched surface layer as a process of accommodation involving also a certain amount of strain retraction, after the main crack front has passed. The deformation field in front of a crack tip and on the crack flanks has been extensively studied and modelled for cases of relatively low strains to local fracture as is characteristic for metals (for references see Xia and Shih[28]). The crack tip deformation fields, including residual strains in the crack flanks for very large local fracture strains, are not well known. Qualitative considerations for large strain flow fields of advancing cracks, with substantial opening angles, would lead to the very large residual stretching strains that have been observed in the present study. Thus, in the process of accommodation of these stretched layers on the crack flanks, it is reasonable to expect that these layers will be required to shorten. While this can, in part, involve some strain retraction, the major form of accommodation is apparently accomplished by the formation of the shallow periodic folding patterns. Then the principal wavelength of these patterns (S_d) and their amplitude (a) of fold heights must depend on the

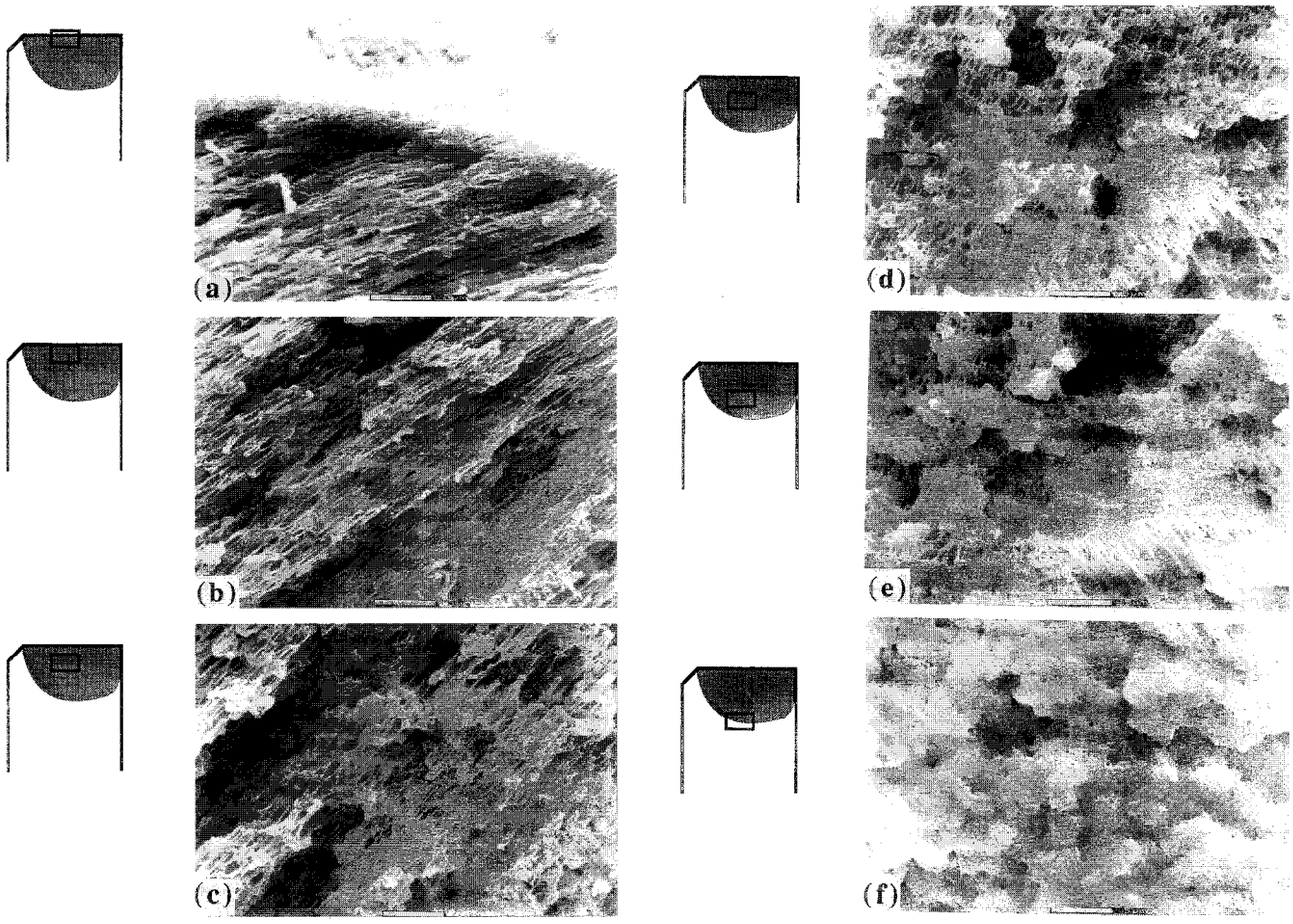

Figure 16 Morphology of the cavities seen from a side view below the crack flank after an Izod test. The inserts next to the micrographs indicate their locations relative to the crack flank. The direction relative to the crack flank in which the micrographs were recorded is schematically shown in *Figure 2*. The direction of crack propagation is from left to right

thickness of the stretched layer and the residual stretches in it. Clearly, the accommodation is aided by a significant out-of-surface compliance of the aligned porous microstructure which we present below.

In an effort to provide support for the hypothesis of surface folding, the stretched porous microstructure was studied in some detail to assess the level of the actual stretching strains (λ) and their principal directions (**S**) beneath the crack flanks. To this end, the Izod tested specimens were cryo-fractured following the method described above and examined under the scanning electron microscope. The morphology of the stretched material at and below the crack flanks could be readily resolved to determine the magnitudes and principal directions of the residual strain field and its variation with distance away from the crack flanks. The micrographs shown in *Figure 16* give a clear representation of the local strain field below the crack flanks. The location of each micrograph with respect to the crack flank is clarified on the left margin of *Figure 16*, and the actual depth is given in *Figure 18*. The gradual change in the orientation of the elongated cavities relative to the crack flank, as shown in *Figure 16*, has also been observed by Speroni *et al.*[17] in rubber-modified polyamide 6 as well as in other materials[29]. In an attempt to identify the toughening mechanisms in polyamide/poly(phenylene oxide) (PA/PPO) blends, Sue and Yee[29] examined the sub-fracture surface morphology of various types of impact specimens. In their system, the modifying phase (PPO) is rigid and does not undergo cavitation. As a result, the particles deform to small strains and eventually debond from the matrix. The orientation of the deformed and debonded particles relative to the flank depicted on their representative micrographs are similar to the detailed morphology shown in *Figure 16*.

The cavities, which serve as convenient markers of the deformation field in these micrographs, are known to originate from the cavitation of the rubbery inclusions; this cavitation produces the observed stress whitening in the deformation zone. These cavities elongate in the direction of the local principal stretch[13]. *Figure 16a* was recorded right below the crack flank and shows that the cavities are elongated and aligned almost parallel to the fracture surface. The micrographs in *Figures 16b–f* clarify the monotonic rotation of the principal stretch axis of the cavities from the interior of the whitened zone to the crack flank. This demonstrates that the direction of the principal stretch axis is nearly parallel to the fracture surface right below the crack flank and undergoes a progressive rotation of nearly 90° going into depth away from the flanks. Clearly, an anisotropic porous material of this constitution at the crack flanks will have a high out-of-surface compliance that should have a low resistance to the periodic folding of the stretched surface layer undergoing the required accommodation.

The variations in the principal residual stretching

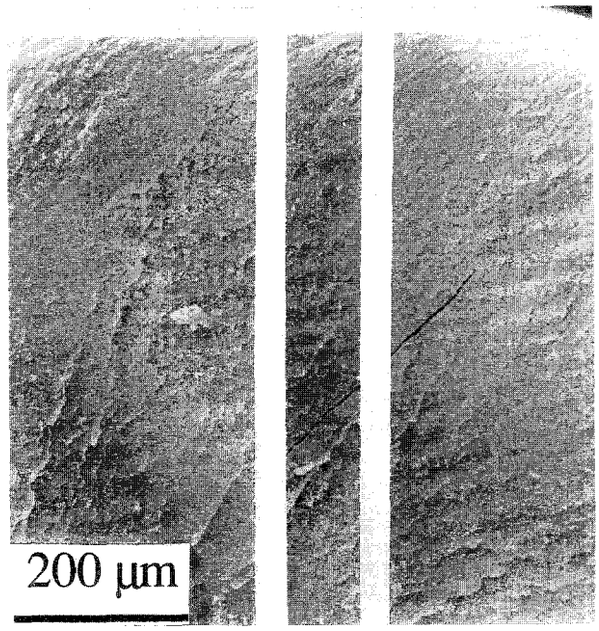

Figure 17 View of sample 8 observed in an ESEM as depicted in *Figure 2*. The indicated rectangular region (between the white strips) was photographed at a magnification of 3200 to determine the data summarized in *Figure 18* (see the text for details). The direction of crack propagation is from left to right

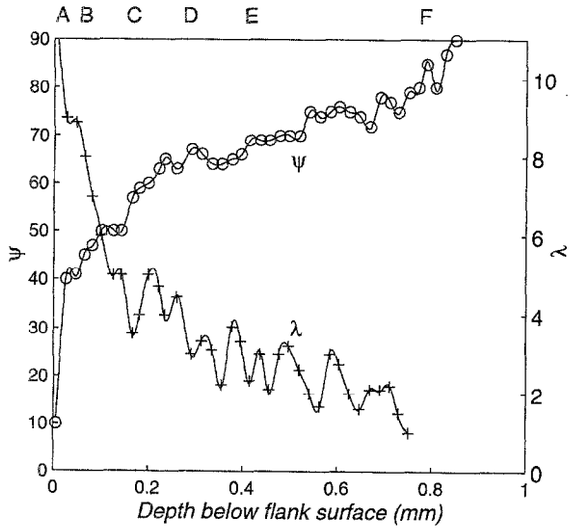

Figure 18 Distribution of magnitudes of draw ratio λ (+) and angle of rotation ψ (O) of the major principal stretch direction, away from the plane of the crack flank. The locations of the micrographs of *Figures 16a–f* are indicated as A–F

strain (λ) and rotation of the orientation of the principal stretch direction (ψ) (measured away from the normal towards the crack flank into the direction of crack propagation) were obtained directly from a series of micrographs recorded below the crack flank in the region between the white strips indicated in *Figure 17*, which shows an overall view of the side cross-section below the crack flank. This series was recorded at a magnification of 3200, generating 45 micrographs which formed a continuous strip 3 m long representing an actual area of 40 μm × 1 mm. The strain induced rotation angle ψ of the principal stretch axis was measured as indicated earlier, and the associated local residual stretch λ was determined by measuring the aspect ratio of the stretched cavities. The results are summarized in *Figure 18*, which also identifies the locations of the micrographs of *Figure 16a–f*[*]. A similar plot was also presented by Speroni *et al.*[17], showing only the variations of the length of the elongated cavities as a function of distance away from the fracture surface. The direction of the local principal deformation was not included in their plot. Such information is important in understanding how the intense deformations and the associated cavities arrive at the crack flanks and how the accommodation of such stretched material might result in deformation instabilities that would produce the striations.

According to *Figure 18*, where both λ and **S** are plotted as a function of depth away from the crack flank, the major axis of the elongated cavities rotates by ~80° in a layer of 1 mm thickness under the crack flank. Within the first 30 μm depth below the flank, the rotation is approximately 30° which amounts to around 35% of the total rotation. Similarly, the aspect ratio of the cavities which represents the local residual stretch diminishes from 10 to 1 within the same 1 mm thickness of flank surface layer. The decrease of stretch within the first 30 μm is around 5, which is about 50% of the total change in the whole stress-whitened zone. Therefore, a thin surface layer (in this case of 30 μm thickness), the 'intense process' zone, below the crack flank is subject to a large rotation of principal stretch axis and large local residual stretch. *Figure 19* is a schematic of the morphology of the cavities below the crack flank, depicting the 'intense process' zone of thickness h and the stress-whitened zone of thickness L. The ratio h/L was found to be typically of the order of 0.03 (as measured in sample 8). That is, effectively 3% of the stress-whitened zone undergoes local residual stretches of the order of 10 parallel to the crack flank. *Figure 20a* shows a hypothetical reconstruction of the processes associated with the passage of the intense deformation zone of crack tip material elements that are then left behind along the crack flanks. If the intensely stretched material layer were unconstrained it would be much longer than the length of the crack flanks. The constraint of the stiffer substrate material, however, forces the stretched layer to shorten. This is accomplished, in part, by some strain retraction, but apparently in a more major way by periodic folding of this thin and stretched surface layer. A certain amount of delamination might be expected below the crack flank under such compressive forces and buckling. However, this is apparently unnecessary because of the rather low 'plucking resistance' of the substrate permitted by the elongated cavities that provide enough flexibility in the direction normal to the crack flank (see *Figure 20b*).

A previous section (Striations in impact and fatigue fracture) summarizes the prominent models proposed for the formation of linear fracture features that are not due to cyclic crack growth on the surface of fatigue fractured semicrystalline polymers. These purely hypothetical models lack supporting evidence[20,21]. The buckling of a

[*] The waviness in the stretch distribution is real and appears to be due to layer-like localization of cavity elongation. The cause of this is not clear. An adiabatic deformation localization is a possible explanation

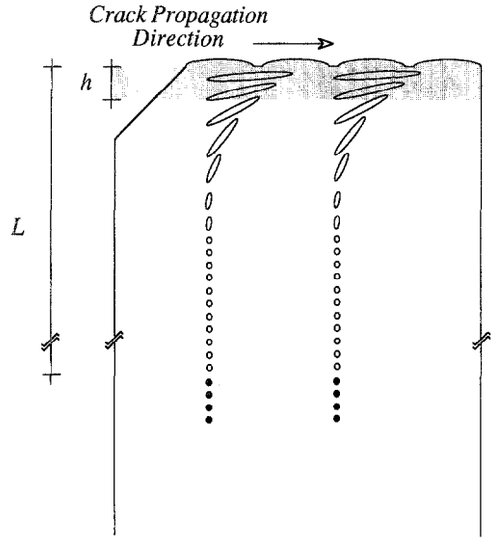

Figure 19 Schematic rendering of the morphology of cavities below the crack flank from the viewpoint described in *Figure 2*. *L* indicates the extent of the stress–whitened region, while *h* indicates the 'intense process' zone. The shaded circles represent uncavitated rubber particles. The undulation on the top edge represents the side view of striations on the fracture surface

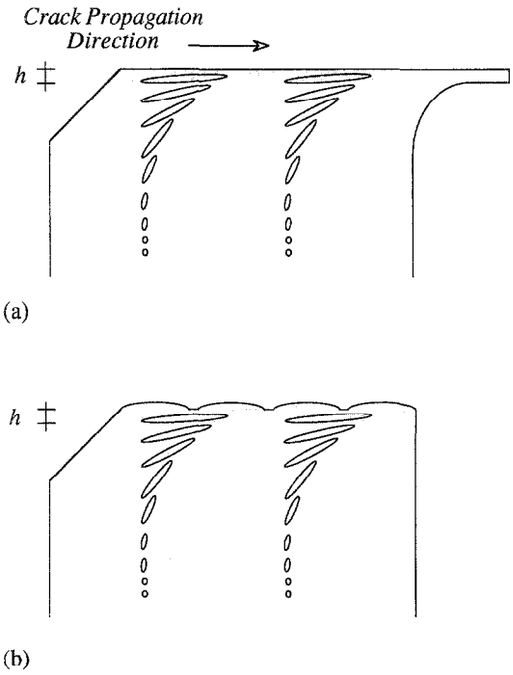

Figure 20 Schematic view in the direction depicted in *Figure 2* of Izod impact samples after fracture: (a) expected hypothetical sample shape that accommodates high local stretches without interacting with the rest of the sample; (b) actual shape where the high local stretches are accommodated by the buckling of the 'intense process' layer

thin and intensely stretched surface layer on the fracture surface of impact tested rubber-modified polyamides may also give more insight into the formation of linear features on fatigue fracture surfaces. Although in a fatigue test the specimen is under continuous cyclic loading and the crack opening angle fluctuates, the deformation induced in the material at every incremental crack propagation step is similar to that in impact testing, at least during the 'opening part' of the cycle. Therefore, at each cycle during fatigue crack propagation through a tough solid, a highly stretched thin region should form along the crack flank which should have a tendency to buckle and fold during the 'closing part' of the cycle. Thus, this could give rise to 'micro-striations' on the fatigue fracture surfaces, at least in material where out-of-surface compliance is large, as in the present case.

Dependence of striation spacing on crack velocity and temperature

The plastic deformation resistance of polymers rises in a predictable manner with increasing strain rate and decreasing temperature. These effects have been studied experimentally in considerable detail in glassy polymers[30], in semicrystalline high density polyethylene[31] and in polyamide 6[32], in the light of molecular level mechanisms. Moreover, most polymers have rather poor thermal diffusivity which can result in a substantial temperature rise at high strain rate deformation and adiabatic strain localization due to the concomitant deformation-induced decrease of plastic resistance. On the other hand, in experiments carried out at different temperatures, a sharp decrease in toughness is observed as the temperature is decreased below a certain level where the material undergoes brittle behaviour, as is clear from the observations related to *Figure 8*. In the light of these responses it was of interest to perform tensile fracture experiments on singly notched specimens at different extension rates and different temperatures to note the effect of these on the striation spacing.

High speed tensile fracture experiments. Examination of the fracture surfaces of the singly notched tension experiments carried out at room temperature showed a decrease in the striation spacing with increasing average crack velocity. To relate this observation to the morphology and orientation of the stretched cavities, the cryo-fractured surfaces of the median plane of specimens fractured at various rates were examined. *Figure 21* shows side views of these singly notched tensile bars of sample 8, where all micrographs were recorded at the same level of magnification for direct comparison. The morphology immediately below the flank changes drastically as the crack growth rate increases from 0.005 to 5 cm s^{-1}. The draw ratios, as measured from the aspect ratio of the elongated cavities that are nearly parallel to the crack flank in the 'intense deformation' zone, increase with increasing crack growth rate. However, at higher deformation rates induced by higher crack velocities, the plastic resistance of the material in the 'intense deformation' zone should increase, if isothermal conditions could be maintained, and result in lower draw ratios. Because of the poor thermal diffusivity of polymers, however, isothermal conditions cannot be maintained and deformation becomes adiabatic instead, resulting in a deformation-induced temperature rise and accounting for the increase in the local draw ratio. Thermal effects in the fracture of rubber-modified polyamides have indeed been encountered by Dijkstra *et al.*[15], who have shown that the rise in temperature within the process zone of a crack tip can become quite high, and possibly even approach the melting point of the matrix. Their samples consisted of rubber-modified polyamide 6 with a melting point of ~215°C. From the morphology below the crack flank they were able to observe a thin layer

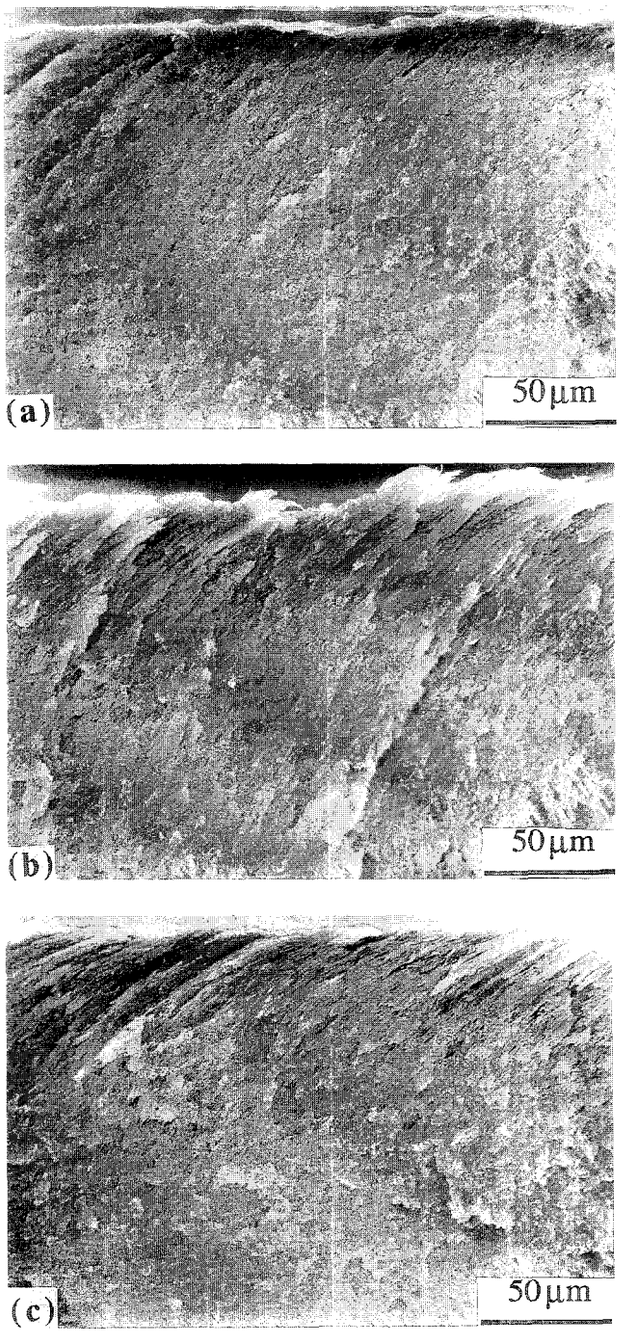

Figure 21 Side view below the crack flank of the single-notched tensile bars of sample 8 tested under uniaxial tensile loading with corresponding crack growth rates of (a) 0.005, (b) 1 and (c) 5 cm s^{-1}

with healed cavities (no cavitation) which they attributed to a local melting process during crack propagation (or more likely due to a rapid healing in the adiabatically heated zone). In the present experiments, such local melting and softening effects below the crack flanks were not observed, probably because of the higher melting point of polyamide 66 (~250°C). However, any local increase of temperature in the crack tip zone would lower the local plastic resistance and localize the deformation there. As a result, the amount of residual stretch should increase while the lightly deformed substrate material encounters a more modest temperature rise. Thus, when the 'intense process' zone accommodates itself to the stiffer substrate, it should undergo folding with a smaller wavelength in the samples with higher crack growth rates. The corresponding fracture surface micrographs of these samples are shown in *Figure 15*, where the observed decrease in striation spacings and other evolving features with increasing crack growth rates are consistent with a higher local rise in temperature in the 'intense process' zone.

Experiments at higher temperatures. The increase in the striation spacing with deformation at higher temperatures must be a consequence of the less localized nature of the deformation as more of the substrate also deforms during crack propagation. Thus, the final draw ratios in the 'intense process' zone are lower and the surface layer folding process does not produce as many striations as it does at lower temperatures. While quantitative confirmation of these explanations is lacking, the observed effects of increasing crack velocity and temperature are in broad agreement with the hypothesis for striation formation advanced above.

A model for striation formation

As presented in our hypothesis above, we view the formation of the striations parallel to the crack front, left behind on the fracture surfaces, as a surface layer buckling process occurring during compressive accommodation of the previously stretched crack front material. We view this as a plastic buckling process where the surface layer with thickness h undergoes a periodic cycloidal buckling under a compressive force P exerted on the layer by the less deformed substrate, as depicted in *Figure 22*. The forces that oppose this buckling are: (1) the plastic bending resistance of the surface layer, which we will treat as if it were an elastic solid with an effective Young's modulus E, and (2) the substrate plucking resistance k which is governed by the regularly cavitated microstructure depicted in *Figure 23*, which we will estimate separately. We offer the following analysis, fashioned as a classical plastic plate on an elastic foundation, only as a means of obtaining a potentially useful scaling law—recognising that the actual problem will no doubt be considerably more complex.

We state the buckling condition of the thin plate on the substrate under the compressive surface load P per unit length by the usual energy method widely used in obtaining an upper bound solution (see den Hartog[33]). For the characteristic length l of the surface layer undergoing buckling, the elastic strain energy of bending, U_b per unit depth (into the figure), is

$$U_b = \tfrac{1}{2}\int_0^l EI\left(\frac{d^2y}{dx^2}\right)^2 dx \qquad (3)$$

while the elastic strain energy of plucking the substrate, U_p per unit depth, by the buckling surface layer as it attempts to partially raise the substrate and partially indent it, is

$$U_p = \tfrac{1}{2}k\int_0^l y^2(x)dx \qquad (4)$$

where k is the foundation elastic spring constant, familiar in problems of beams and plates on elastic foundations (see again den Hartog[33]). Finally the work done, W per

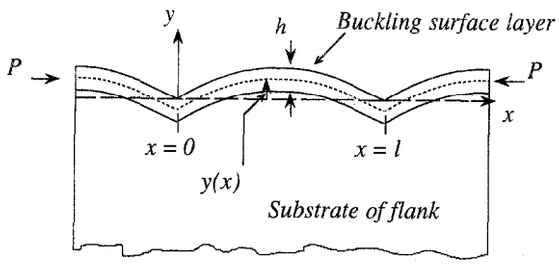

Figure 22 Schematic of the buckling of the surface layer of thickness h that results in the fracture surface striations. The variables used in the model are denoted in the figure

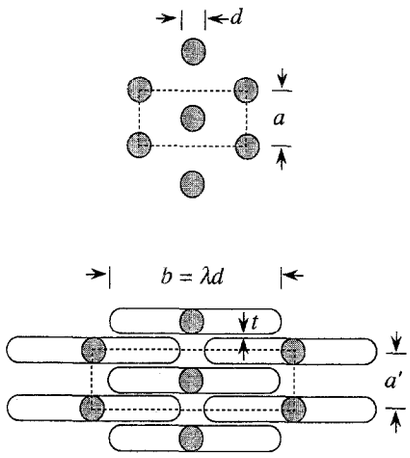

Figure 23 Schematic of seven particles hexagonally packed before and after large strain deformation below the crack flank. The elongated cavities would be aligned nearly parallel to the fracture surface. The rubber particles are drawn in the deformed morphology as uncavitated to indicate that the change in the width of the specimen is negligible as explained in ref. 13

unit depth, by the compressive load P during the impending development of the buckling shape is

$$W = \frac{P}{2}\int_0^l \left(\frac{dy}{dx}\right)^2 dx \tag{5}$$

In all of the above, the displacement $y(x)$ normal to the surface is measured from the initially flat neutral plane of the surface plate as depicted in *Figure 22*. We note, moreover, that since there are no net out-of-surface tractions applied to the plate

$$k\int_0^l y(x)dx = 0 \tag{6}$$

By the principle of virtual work, the work done by the compressive load must equal the sum of the two other forms of energy, i.e.

$$W = U_b + U_p \tag{7}$$

In the spirit of seeking a workable upper bound solution, we take the buckled shape of the plate as a simple second-order parabola as

$$y = A + Bx + Cx^2 \tag{8}$$

and impose the condition of symmetry as $y = y_0$ at $x = 0$ and $x = l$, together with the condition of no net traction

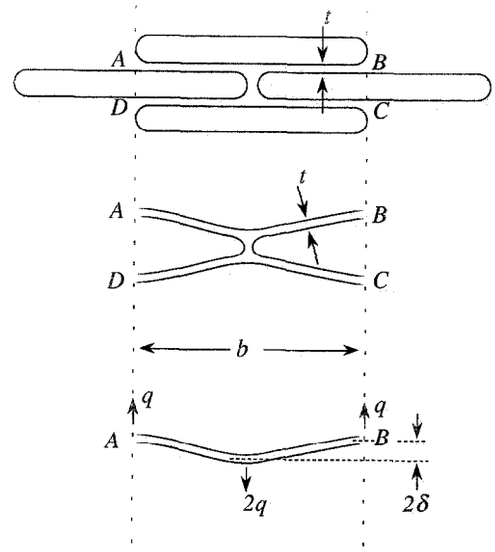

Figure 24 The matrix ligaments around the elongated cavities shown at the top of this schematic were treated as elastic beams to estimate the plucking resistance of the porous substrate

given by equation (6) above, to obtain

$$y = C\left[\frac{l^2}{6} - lx + x^2\right] \tag{9}$$

Substitution of equation (9) into equations (3)–(5) and use of equation (7), with some simplifications, gives the second-order simple differential equation relating l^2 to P as:

$$kL^2 - 30PL + 360E'I = 0 \qquad (L = l^2) \tag{10}$$

In equation (10) we have replaced E with E' which we now interpret as the strain hardening rate $E' = dY/d\epsilon$, as is usually done for problems involving plastic buckling.

In normal practice equation (10) would be used to solve for the buckling load in a given geometrically defined system. Here we will invert the problem. We assume that buckling sets in while the surface layer is in a state of reverse plastic deformation and that P is the plastic yield load. We then use equation (10) to solve for L. To proceed further, we need to relate the substrate plucking resistance to the substrate porous microstructure and relate $E'I$ to the microstructure of the surface layer.

These relations can be readily obtained from elementary beam theory and are developed with the help of *Figures 23* and *24* and the Appendix. The result is:

$$k = \frac{E}{4\lambda^4 d}\left(\frac{\pi}{4\lambda}\frac{(1-c)}{c}\right)^3 \tag{11}$$

$$E'I = \frac{(dY/d\epsilon)h^3}{12\left(1 + \frac{4\lambda}{\pi}\frac{c}{1-c}\right)} \tag{12}$$

where c is the volume fraction of the initially spherical rubber particles of diameter d, which are considered to have cavitated while reaching the crack tip, leading to the elongated parallel cavities of *Figures 23* and *24*; these cavities have been stretched out to a principal extension ratio of λ which also becomes nearly parallel to the crack flank surfaces, as the stretched material is left behind on the crack flanks.

The two roots of equation (10) are

$$L_{1,2} = 15\frac{P}{k}\left[1 \pm \sqrt{1 - \frac{360}{225}\frac{E'Ik}{P^2}}\right] \tag{13}$$

where

$$\frac{P}{k} = \frac{4Yhd\lambda^4}{E\beta} \tag{14}$$

$$\frac{E'I}{k} = \frac{h^3 d\lambda^4}{4\beta}\frac{(dY/d\epsilon)}{E} \tag{15}$$

$$\beta = \left(1 + \frac{4\lambda}{\pi}\frac{c}{(1-c)}\right)\left(\frac{\pi}{4\lambda}\frac{(1-c)}{c}\right)^3 \tag{16}$$

We now note that for a typical case of $c = 0.1$, $\lambda = 8$, with $(dY/d\epsilon)/E = O(Y/E) = O(0.04)$, $d/h = O(0.2)$, giving $\beta = 1.47$, the second term under the radical in equation (13) is very much smaller than unity. This permits obtaining two positive solutions for the wavelength of the striation spacing as:

$$l_1 = \frac{\sqrt{3}}{2}h\sqrt{\frac{(dY/d\epsilon)}{Y}} \tag{17}$$

$$l_2 = \lambda^2 h\sqrt{120\left(\frac{Yd}{Eh\beta}\right)} \tag{18}$$

Of these two solutions, the first is for the range of properties where the substrate plucking resistance dominates and the plastic bending resistance is negligible, while the second is for the complementary one where the plastic bending resistance of the surface layer dominates and the substrate plucking resistance is negligible.

For the typical case properties given above with $(dY/d\epsilon)/Y \approx O(1.0)$ we obtain

$$l_1 = \frac{\sqrt{3}}{2}h \tag{19}$$

$$l_2 = 16.4h \tag{20}$$

While our idealization of the problem has been severe, we find the second predicted wavelength far too long to be meaningful and conclude that our problem is governed primarily by the substrate plucking resistance. This leads to the first predicted wavelength for which the geometrical effects of the microstructure do not enter; but the important result established is that reduction of the plastic resistance Y, by whatever cause, will increase the striation spacing—noting that the strain hardening rate $dY/d\epsilon$ should be primarily temperature and strain rate independent. This is, of course, what has been observed.

CONCLUSIONS

To investigate the fracture process in rubber-modified polyamide 66, Izod flexural bars with varying particle size and rubber content were tested at different temperatures. The fractured samples were examined in an SEM to reveal the morphology of the fracture surfaces and process zone below the crack flanks. The features detected on the fracture surfaces of the samples varied significantly, depending on the level of toughness. These features consisted of a patchy but generally smooth surface on brittle samples, striations on ductile ones and a combination of the two on samples in the transition zone. The microstructural processes of fracture involved in crack growth of these toughened polyamides consist of: cavitation of rubber particles within the process zone; stretching and rotation of cavities in the direction of the local major principal strain axis; and formation of striations via folding of the stretched fracture surface by plastic buckling. The spacing between the striations increased with increasing temperature, particle size, rubber content and deformation rate. These variations were attributed to temperature and rate dependence of the viscoplastic properties of the matrix material and the anticipated adiabatic localization of deformation for high crack velocities. A model for striation formation was developed based on plastic buckling of a thin plate on an elastic foundation which is in reasonable agreement with observations—particularly the effect of temperature on the striation spacing. The proposed model of buckling of thin surface layers to explain the formation of striations on the fracture surface can also be a possible explanation for the formation of the well-known fatigue striations that cannot be associated with cyclic crack growth ('microstriations').

ACKNOWLEDGEMENTS

Early stages of this research were supported by NSF/MRL through the Center for Materials Science and Engineering at MIT under DMR-90-22933 and by a DuPont Company Graduate Fellowship for OKM, for which we are grateful to Dr D. Huang of that company. We also acknowledge the assistance of Ms Jill Sherwood in image analysis.

REFERENCES

1 Flexman, E. A. *Polym. Eng. Sci.* 1979, **19**, 564
2 Hobbs, S. Y., Bopp, R. C. and Watkins, V.H. *Polym. Eng. Sci.* 1983, **23**, 380
3 Wu, S. *J. Appl. Polym. Sci.* 1988, **35**, 549
4 Borggreve, R. J. M. and Gaymans, R. J. *Polymer* 1989, **30**, 63
5 Oshinski, A. J., Keskkula, H. and Paul, D. R. *Polymer* 1992, **33**, 267
6 Majumdar, B., Keskkula, H. and Paul, D. R. *Polymer* 1994, **35**, 1399
7 Dijkstra, K., ter Laak, J. and Gaymans, R. J. *Polymer* 1994, **35** 332
8 Borggreve, R. J. M., Gaymans, R. J., Schuijer, J. and Ingen-Housz, J. F. *Polymer* 1987, **28**, 1489
9 Wu, S. *Polymer* 1985, **26**, 1855
10 Muratoğlu, O. K., Argon, A. S. and Cohen, R. E. *Polymer* 1995, **36**, 2143
11 Keller, A. *J. Polym. Sci.* 1959, **35**, 361
12 Scott, R. G. *J. Appl. Phys.* 1957, **28**, 1089
13 Muratoğlu, O. K., Argon, A. S., Cohen, R. E. and Weinberg, M. *Polymer* 1995, **36**, 921
14 Lin, L and Argon, A. S. *Macromolecules* 1992, **25**, 4011
15 Dijkstra, K., ter Laak, J. and Gaymans, R. J. *Polymer* 1994, **35**, 315
16 Wilson, F. C. *Mater. Res. Soc. Symp., Boston* 1989, p. 413
17 Speroni, F., Castoldi, E., Fabbri, C. and Casiraghi, F. *J. Mater. Sci.* 1989, **24**, 2165
18 Ward, I. M. 'Mechanical Properties of Solid Polymers', 2nd edn, John Wiley & Sons, New York, 1990
19 Bretz, P. E., Hertzberg, R. W. and Manson, J. A. *J. Mater. Sci.* 1981, **16**, 2070

20 Hahn, M. T., Hertzberg, R. W. and Manson, J. A. *J. Mater. Sci.* 1986, **21**, 39
21 White, J. R. and Teh, J. W. *Polymer* 1979, **20**, 764
22 Skibo, M. D., Hertzberg, R. W. and Manson, J. A. *J. Mater. Sci.* 1977, **12**, 1531
23 Hertzberg, R. W., Skibo, M. D. and Manson, J. A. *J. Mater. Sci* 1978, **13**, 1038
24 Schwarze, F. and Staverman, A. J. in 'Die Physik der Hochpolymeren' (Ed. H. A. Stuart), Springer, Berlin, 1956, Vol. 4, p. 165
25 Doyle, M. J., Maranci, A., Orowan, E. and Stork, S. T. *Proc. Roy. Soc.* 1972, **A329**, 613
26 Hull, D. in 'Polymeric Materials' (Eds E. Baer and S. V. Radcliffe), ASM, Metals Park, OH, 1975, p. 487
27 Williams, J. G. 'Fracture Mechanics of Polymers', 1st edn, John Wiley & Sons, New York, 1984
28 Xia, L. and Shih, C. F. *J. Mech. Phys. Solids* 1995, **43**, 233
29 Sue, H. J. and Yee, A. F. *J. Mater. Sci.* 1989, **24**, 1447
30 Argon, A. S. and Bessonov, M. I. *Phil. Mag.* 1977, **35**, 917
31 G'Sell, C. and Dahoon, A. Personal communication, 1994
32 Lin, L. and Argon, A. S. *Macromolecules* 1994, **27**, 6903
33 den Hartog, J. P. 'Advanced Strength of Materials', 1st edn, McGraw-Hill, New York, 1952

APPENDIX: GEOMETRICAL PROPERTIES OF BUCKLING SURFACE LAYER, AND SUBSTRATE PLUCKING STIFFNESS

To determine the properties related to the microstructure, we first idealize the microstructure in two-dimensional form as a hexagonally arranged set of cylindrical rubber rods of diameter d. The large strain extension is in-plane strain resulting in a local principal extension ratio of λ, elongating the surrounding of a cavitated rubber rod as a slot of thickness d and length $b = \lambda d$ as depicted in *Figure 23*. In this figure for geometrical clarity we show the rubber particles intact and the cavity having been formed by debonding. The fact that the cavity will upon stretching retain its initial thickness is established from direct observation and relates to the crystallite morphology of the matrix around the particle which we have discussed in detail earlier (see Muratoğlu *et al.*[13]).

Noting that the initial volume fraction of the rubbery component is

$$c = \frac{\sqrt{3}\pi}{6}\left(\frac{d}{a}\right)^2 \tag{A1}$$

we obtain, by simple geometrical considerations of conservation of matrix volume, the thickness t of the matrix ligaments depicted in *Figure 23* as:

$$t = \frac{\pi d}{4\lambda}\frac{(1-c)}{c} \tag{A2}$$

Then, the required substrate plucking resistance k (foundation stiffness) can be obtained with the help of *Figure 24* with similar ease from simple beam theory as:

$$k = \frac{(2q/\lambda d)}{2\delta} \tag{A3}$$

$$\delta = \frac{4q}{E}\left(\frac{\lambda d}{t}\right)^3 \tag{A4}$$

where the numerator of equation (4) is the average plucking stress and 2δ the corresponding plucking displacement as shown in *Figure 24*. This gives immediately

$$k = \frac{E}{4\lambda^4 d}\left(\frac{\pi}{4\lambda}\frac{(1-c)}{c}\right)^3 \tag{A5}$$

The effective in-plane Young's modulus E', or more appropriately the tensile or compressive strain hardening rate $(\mathrm{d}Y/\mathrm{d}\epsilon)'$, is given by a direct rule of mixtures, appropriate for the in-plane direction

$$E' = c'E \Rightarrow (\mathrm{d}Y/\mathrm{d}\epsilon)' = c'(\mathrm{d}Y/\mathrm{d}\epsilon) \tag{A6}$$

where c', the material volume fraction in the stretched state, can be given as

$$c' = \frac{2t}{a'} = \frac{1}{1+\dfrac{4\lambda}{\pi}\dfrac{c}{(1-c)}} \tag{A7}$$

giving

$$E' = \frac{E}{1+\dfrac{4\lambda}{\pi}\dfrac{c}{(1-c)}} \Rightarrow (\mathrm{d}Y/\mathrm{d}\epsilon)'$$

$$= \frac{(\mathrm{d}Y/\mathrm{d}\epsilon)}{1+\dfrac{4\lambda}{\pi}\dfrac{c}{(1-c)}} \tag{A8}$$

Moreover, by similar arguments, the in-plane effective plastic resistance load P (per unit thickness) is obtained as

$$P = Yc'h = \frac{hY}{1+\dfrac{4\lambda}{\pi}\dfrac{c}{(1-c)}} \tag{A9}$$